

Turing-Type Patterns on Electrode Surfaces

Yong-Jun Li, Julia Oslonovitch, Nadia Mazouz, Florian Plenge, Katharina Krischer,* Gerhard Ertl

We report stationary, nonequilibrium potential and adsorbate patterns with an intrinsic wavelength that were observed in an electrochemical system with a specific type of current/electrode-potential ($I-\phi_{DL}$) characteristic. The patterns emerge owing to the interplay of a self-enhancing step in the reaction dynamics and a long-range inhibition by migration currents rather than by diffusion. Theoretical analysis revealed that this self-structuring of the electrode occurs in all electrochemical systems with an S-shaped $I-\phi_{DL}$ characteristic in wide and well-accessible parameter ranges. This unusual pattern-forming instability in electrochemical systems has all the characteristics of the mechanism proposed by Turing in 1952 in the framework of an early theory of morphogenesis. Our finding might account for structure formation in certain biological systems that have gradients in the electric potential and may open new paths for fabricating patterned electrodes.

Nearly half a century ago, Turing (1) developed a theory of morphogenesis, in which stationary concentration patterns may develop in an open system containing two reacting substances provided that one of them diffuses much faster than the other one (2, 3). Today, Turing's mechanism is considered to be a central source for the occurrence of coherent patterns in nonequilibrium systems (2–4). Still, the experimental verification of chemical Turing structures could be achieved only in exceptional cases. Transient patterns that were attributed to a Turing instability were observed in the development of colloidal growth in a supersaturated solution (5). Stationary chemical Turing structures were realized only quite recently and only for one specific chemical oscillator (6–8), because in aqueous solution diffusion coefficients of small molecules do not differ substantially from each other. In the experiments, sufficient differences of the mobilities were achieved by using a macromolecular indicator that partially immobilizes the "critical" species by reversible complexation (9). In recent theoretical work it was suggested that a certain class of electrochemical systems might exhibit Turing-type structures without suffering from the restrictions on the different rates of the transport processes (10). In these systems, the electrode potential takes on the role of the rapidly diffusing species, and the associated transport process is migration, that is, the motion of ions under the influence of an electric field. Here we present experimental evidence for the formation of these stationary, migration-induced nonequilibrium

structures in large parameter ranges. Indeed, the structures were found to develop whenever the reaction dynamics allowed for its occurrence, which substantiates the conjectured widespread existence of Turing-type patterns in electrochemical systems.

The electrochemical Turing structures are predicted to exist in systems with a bistable, S-shaped (I) current-potential ($I-\phi_{DL}$) curve. In view of possible applications, as well as their relevance for modeling biological processes, the most important electrochemical systems of the S type seem to be those in which a first-order phase transition of an organic adsorbate is coupled with a faradaic reaction of some electroactive species.

As a representative of such systems, we used the periodate reduction on Au(111) electrodes in the presence of camphor. In the experiments, Au(111) single crystals as well as 50-nm-thick Au film electrodes with a preferential (111) orientation were used. The single crystals were rotated in a hanging meniscus geometry. The film electrodes were used in connection with a surface plasmon microscope (12) to study the lateral distribution of the double-layer potential and of adsorbed camphor (Fig. 1).

Camphor adsorbed on Au(111) electrodes exhibits two first-order phase transitions upon variation of the electrode potential (13). In a cyclic voltammogram (CV), the phase transition manifests itself in a pair of needle-like peaks (Fig. 2A). Between the peak pairs a condensed, well-ordered camphor film exists. At more negative potentials, the camphor coverage is very low, while the state of the adsorbate at positive potentials beyond the range for the condensed film is not yet known. The small hystereses between the respective anodic and cathodic peaks are caused by the finite nucleation rate of the

respective thermodynamically stable phase.

Periodate (IO_4^-) in a camphor-free electrolyte is reduced on Au(111) in the potential range that we consider here, as reflected by the CV of Fig. 2B. In the presence of camphor, however, IO_4^- reduction is inhibited when the condensed camphor film covers the electrode, i.e., between about -300 to -700 mV (Fig. 2C). The phase transitions accompanying the formation or dissolution of the condensed camphor film, respectively, cause the hystereses in the CV, which also persist under stationary conditions. The bistability I in the more negative (i.e., cathodic) potential range exhibits the shape of an S, whereas the other bistability II in the more positive potential range is of the Z type.

The current-voltage ($I-U$) characteristic is determined not only by the interfacial processes, i.e. adsorption/desorption and reaction, respectively, but also by the electric properties of the whole electrochemical cell: The external voltage U is composed of the potential drop across the double layer, ϕ_{DL} (responsible for the interfacial processes), plus the ohmic resistance R in the electrolyte between working and reference electrode

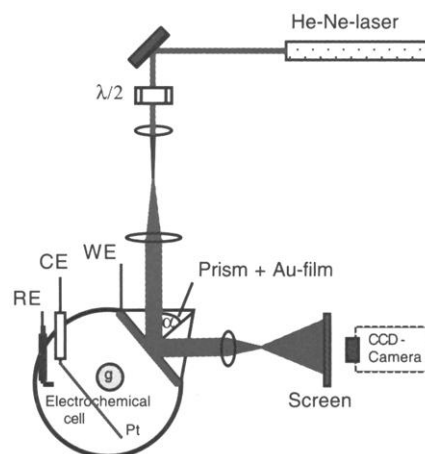
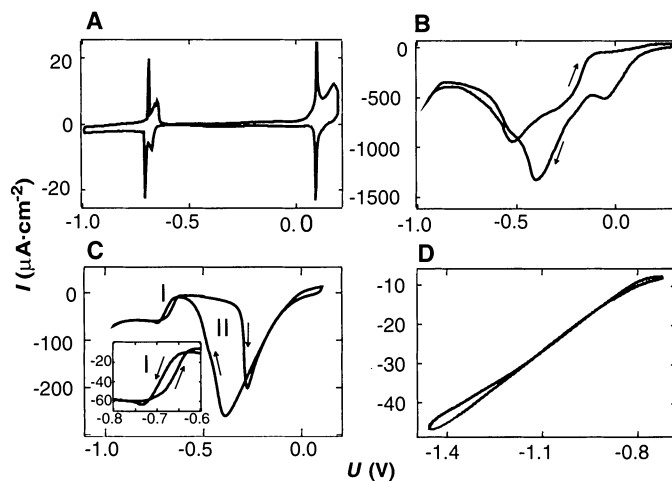


Fig. 1. Experimental setup for imaging patterns at the electrode/electrolyte interface by means of surface plasmon microscopy (top view): working electrode [a ~ 50 -nm-thick Au film evaporated onto a glass plate (B270) that was brought into optical contact with a glass prism; the area of the WE exposed to the electrolyte was 8 mm by 30 mm]. CE: counter electrode (a Pt wire, wound to a spiral of the same size as the working electrode and placed parallel to it at a distance of ~ 4 cm). RE: Hg/Hg₂SO₄ reference electrode. (All voltages are given with respect to this reference electrode). g: gas inlet for Ar bubbling. (The mass transport was achieved by means of gas bubbling.) The electrode was irradiated from behind by a broadened, p-polarized He-Ne laser beam and imaged with a charge-coupled device (CCD) camera. Before each experiment, the film was flame-annealed several times in a gentle butane flame, resulting in a film with a high degree of (111) facets, as revealed by electrochemical characterization.

Fritz-Haber-Institut der Max-Planck-Gesellschaft, Faradayweg 4-6, D-14195 Berlin, Germany.

*To whom correspondence should be addressed. E-mail: krischer@fhi-berlin.mpg.de

Fig. 2. Cyclic voltammograms of an Au electrode in contact with different electrolytes: (A) 5 mM camphor and 50 mM NaClO_4 ; (B) 5 mM NaIO_4 and 100 mM NaClO_4 ; (C) 5 mM camphor, 32 mM NaClO_4 , and 5 mM NaIO_4 ; and (D) 5 mM camphor, 0.5 mM NaClO_4 , and 0.5 mM NaIO_4 . Scan rate, 50 mV/s. In (A) a bulk Au(111) electrode was used in the hanging meniscus geometry (with the film electrodes, the phase-transition peaks were less pronounced); (B to D) were obtained with a Au film electrode. In the case of the Au(111) bulk electrode, the inhibition of IO_4^- reduction by camphor was in general stronger than with the film electrodes, and better defined transport of rotating electrodes minimized the differences in the back-and-forth scan outside the bistable regions, especially in the part positive to the Z region in (C).



multiplied by the current I : $U = \phi_{\text{DL}} + IR$. For negligible current, as is the case in the presence of camphor alone without IO_4^- in the potential range between the two phase transitions (compare with Fig. 2A), $U \approx \phi_{\text{DL}}$. In the case of IO_4^- reduction, however, in order to establish a certain reduction current I as determined by an associated ϕ_{DL} , the applied voltage has to be more negative by IR . Thus, the actual shape of the I - U characteristic is affected by the cell resistance, which may be modified, e.g., by the electrolyte composition. When the IR drop exceeds the

width of the bistable region in the I - ϕ_{DL} curve (i.e., the width of the coexistence range of the two phases when the current is plotted as a function of ϕ_{DL} by correcting the respective U data by IR), the S region turns into a single-valued, sigmoidal I - U characteristic. Such a situation is shown in Fig. 2D, where the resistance of the cell had been increased by lowering the electrolyte concentrations. The critical IR drop, which turns the bistable into a monostable characteristic, may only be on the order of 10 mV.

Beyond this critical IR drop, the I - U curve

has a positive slope throughout and does not contain any hint of an unstable situation. However, it is exactly under such conditions that we observed a spatial symmetry breaking of the adsorbate coverage and the double-layer potential distribution. When monitoring these properties by means of surface plasmon microscopy during a voltage scan in the single-valued S region, we observed the spontaneous formation of “spotlike” patterns at voltages that correspond to intermediate current values that cannot be stably adjusted under conditions in which the system exhibits bistability. Examples of such measurements, in which one, two, or three spots formed, are shown in Fig. 3, A to C, respectively. The patterns remain unchanged when the voltage was fixed at a certain value within the “patterned region.” These stationary nonequilibrium patterns are also formed if the potential is stepped into this region. We did not observe the coexistence of a homogeneous state and a stationary pattern. The number of spots depended on the reaction conditions, although the parameters for the formation of either two or three spots seemed to be rather close together.

In the specific resistance versus external voltage parameter plane, the stationary patterns exist in a V-shaped region that opens toward large overvoltage (i.e., for reduction reactions in the negative direction) and larger resistance (Fig. 4A). This trend reflects the more stretched I - U curve for a lower conductivity of the electrolyte. For resistivities smaller than the tip of the “V,” the I - U curve was bistable, and only transient concentration waves during the transition between the two phases were observed.

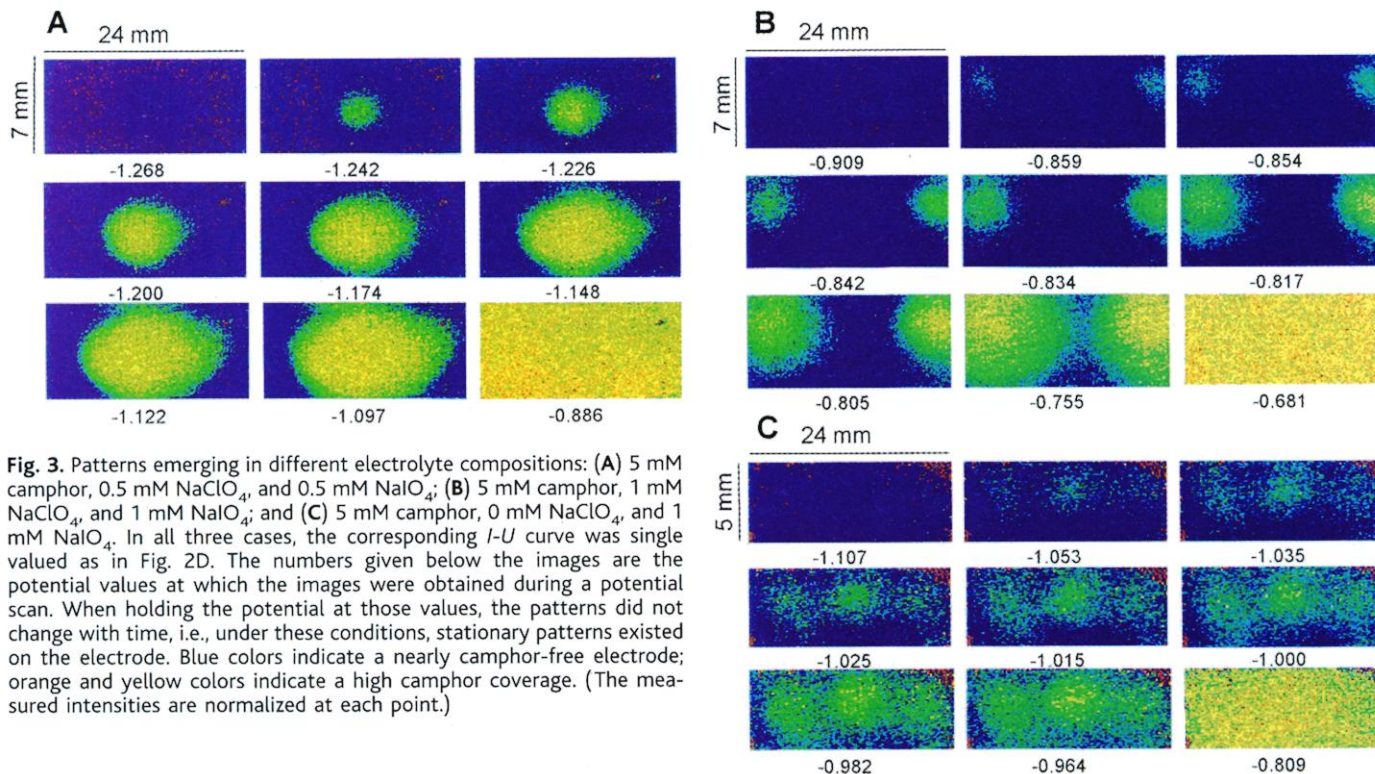


Fig. 3. Patterns emerging in different electrolyte compositions: (A) 5 mM camphor, 0.5 mM NaClO_4 , and 0.5 mM NaIO_4 ; (B) 5 mM camphor, 1 mM NaClO_4 , and 1 mM NaIO_4 ; and (C) 5 mM camphor, 0 mM NaClO_4 , and 1 mM NaIO_4 . In all three cases, the corresponding I - U curve was single valued as in Fig. 2D. The numbers given below the images are the potential values at which the images were obtained during a potential scan. When holding the potential at those values, the patterns did not change with time, i.e., under these conditions, stationary patterns existed on the electrode. Blue colors indicate a nearly camphor-free electrode; orange and yellow colors indicate a high camphor coverage. (The measured intensities are normalized at each point.)

These waves did not nucleate at or close to positions at which the spots formed but usually near one of the two smaller sides of the rectangular electrode.

To rationalize the formation of the stationary patterns, we first consider the dynamics of the homogeneous (i.e., only time-dependent) system. If one starts with a camphor-containing

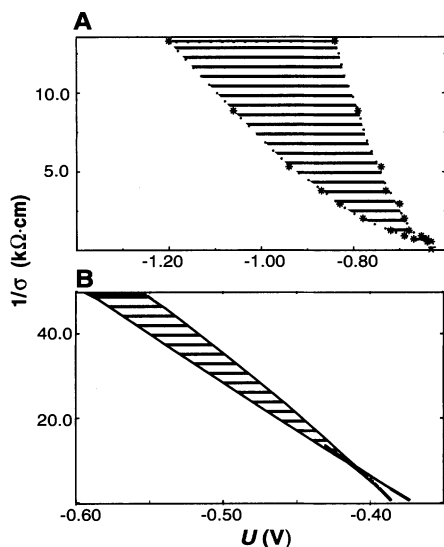


Fig. 4. Existence region of the patterns in the electrolyte resistance versus external voltage plane. (A) Experimental diagram. The electrolyte resistance, $1/\sigma$, was calculated from the ionic concentrations c_i ,

according to $\sigma = \left(\frac{FD}{RT}\right) \sum_i (n_i^2 c_i)$ (F : Faraday's

constant; D : 10^{-5} cm^2/s ; R : gas constant; T : absolute temperature; n_i : charge number of the ionic species i ; c_i : concentration of the ionic species; i : Na^+ , IO_4^- , or ClO_4^-). Electrolytes: 5 mM camphor, 0.5 mM NaIO_4 , x mM NaClO_4 . (B) Theoretical diagram. The diagram was calculated with the dimensionless version (9)

of Eqs. (1) and (2) $\frac{\partial \theta}{\partial t} = \mu f(\theta, \phi_{\text{DL}}) + \frac{\partial^2 \theta}{\partial x^2}$,

$$\frac{\partial \phi_{\text{DL}}}{\partial t} = g(\theta, \phi_{\text{DL}}) - \frac{d}{\beta} \left(\frac{\partial \phi}{\partial z} \Big|_{z=-1} + (U - \phi_{\text{DL}}) \right),$$

where $f(\theta, \phi_{\text{DL}}) = (1 - \theta)e^{-0.025\phi_{\text{DL}} + 2.4\theta} - 0.5\theta e^{+0.025\phi_{\text{DL}} - 2.4\theta}$, $g(\theta, \phi_{\text{DL}}) = -\kappa(1 - \theta)e^{-\phi_{\text{DL}}} + \frac{d}{\beta}(U - \phi_{\text{DL}})$, $\mu = 25$, $\kappa = 10$, $\beta = 10$. $z = -1$ is the boundary between electrolyte and electrode.

$\frac{\partial \phi}{\partial z}$ was obtained from the solution of Laplace's equation $\Delta \phi = 0$, subject to periodic boundary conditions in x (parallel to the 1D electrode), and to $\phi(x, t, z = 0) = 0$, $\phi(x, t, z = -1) = \phi^0$, $U = \phi_{\text{DL}}(x) + \phi(x)|_{z=-1}$. (Laplace's equation governs the potential distribution in the electrolyte. The electrolyte was assumed to be 2D, $z = 0$ being the end of the domain opposite to the WE.) The physical quantity $1/\sigma$ was recalculated from $d = (L\sigma)/(2\pi DC)$ with $L = 1$ cm, $D = 10^{-5}$ cm^2/s , and $C = 10$ $\mu\text{F}/\text{cm}^2$. U is given with respect to the point of zero charge.

solution at a negative potential (e.g., close to the negative turning point in Fig. 2, A or C), an increase of the potential to more positive values causes an increase of the equilibrium concentration of adsorbed camphor. The rise in coverage continues until at a critical coverage, a first-order phase transition to a dense film with high camphor concentration takes place, owing to the operation of attractive interactions between the adsorbates. Thus, reduction of IO_4^- will be inhibited, causing a decrease of the current density I . Under potentiostatic conditions, this inhibition prompts a shift of ϕ_{DL} toward more cathodic (i.e., negative) values. Camphor will now desorb more readily, and a negative-feedback loop is created: Because the build-up of the camphor film is associated with a decrease of the current density for periodate reduction, the response of the system (through the double-layer potential) limits the growth of the camphor film. Thus, we can identify the camphor coverage with the activator and the electrode potential with the inhibitor in an activator/inhibitor system. This conclusion can, in fact, be generalized to all electrochemical systems exhibiting S-shaped current-potential characteristics.

A general model of the spatiotemporal self-organization in such systems can be described with two equations (10). Equation 1 extends the homogeneous (i.e., local) dynamics of the concentration θ of the activator ($\hat{=}$ camphor coverage) as described by the function $f(\theta, \phi_{\text{DL}})$ to spatial spreading by diffusion as characterized by the diffusion constant D :

$$\frac{\partial \theta}{\partial t} = f(\theta, \phi_{\text{DL}}) + D \nabla^2 \theta \quad (1)$$

Equation 2 is the central expression for pattern formation in electrochemical systems, which follows from local charge balance (14):

$$C \frac{\partial \phi_{\text{DL}}}{\partial t} = g(\phi_{\text{DL}}, \theta) - \sigma \left(\frac{\partial \phi}{\partial z} \Big|_{z=\text{WE}} + \frac{U - \phi_{\text{DL}}}{\beta} \right) \quad (2)$$

where C is the specific double-layer capacitance and σ is the specific conductivity of the electrolyte, which together with the geometric factor β determines the cell resistance per unit electrode area. U is the externally applied voltage, ϕ is the electric potential in the electrolyte, and z is the coordinate normal to the electrode. In analogy to reaction-diffusion equations, the local dynamics of the electrochemical system is comprised in the function $g(\phi_{\text{DL}}, \theta)$, and the second term on the right-hand side of Eq. 2 is the counterpart to the diffusion term in Eq. 1; it represents spatial coupling between different locations on the electrode owing to an inhomogeneous potential distribution. Diffusion is thus replaced by migration.

The key element for spontaneous spatial symmetry breaking in an activator-inhibitor system is the ratio of the characteristic rates of the transport processes associated with the activator and inhibitor variable. This rate determines the effective ranges of the respective influence. For the sake of simplicity, consider a one-dimensional (1D) electrode of length L . Then, the ratio of the rate of migration and diffusion is given by a dimensionless constant $d \propto (L\sigma)/(DC)$. L , σ , and C are readily accessible. Taking 10^{-5} cm^2/s as an upper bound for D and typical values for the other three parameters, d results to be on the order of 10^3 to 10^4 . Thus, the potential spreads far more rapidly than the coverage does. This is exactly the situation that leads to a destabilization of the homogeneous state and thus to the formation of patterns. For a 1D electrode with periodic boundary conditions, model Eqs. 1 and 2 possess stationary periodic solutions (10). They bifurcate from the homogeneous state, and their wavelength depends solely on the rate constants of the model [and not on the size of the electrode as one might conjecture because it enters the parameter d (10)]. Thus, the patterns have all of the characteristics of Turing patterns. Plotting the location of the calculated Turing-type instability in the $\sigma^{-1} - U$ parameter plane, a similar V-shaped region is obtained as in the experiment (despite the different electrode geometry) (Fig. 4B). However, other aspects of the experiments require further investigation, such as why we were unable to observe stripe patterns or which mechanisms govern pattern selection on 2D electrodes.

In the presence of a phase transition, as in our experiment, the flow of adsorbed molecules due to a gradient in the chemical potential of the adsorbate does not yield a Fickian diffusion term but a more complicated one where D depends on the adsorbate coverage. This nonlinear diffusion induces spatial instabilities that generate patterns on the nanometer scale (15–18), which makes the detailed mathematical description of our experimental systems more complicated. However, to understand the origin of the instability of the observed patterns, which are of macroscopic dimensions, it is not necessary to take nonlinear diffusion into account. The estimation $d \gg 1$ remains valid also in this case, ensuring that migration still provides long-range inhibition. The latter inevitably leads to a destabilization of the uniform state of an activator-inhibitor system.

A large variety of organic adsorbates (19) exhibit a first-order phase transition as a function of the electrode potential. By adding an electroactive species, the faradaic reaction will destabilize the homogeneous adsorbate layer in the same way as periodate reduction destabilizes the uniform camphor layer. This fact points to a prospective exploitation of the pattern-forming mechanism to manufacture structured electrodes, e.g.,

ones that are similar to those being developed for the fabrication of (bio)sensors. Note that the wavelength is determined by the different rate constants, which can be varied, e.g., by choosing different faradaic reactions or adsorbates or by changing the temperature. In general, the faster the faradaic reaction and the dynamics of the adsorbate system, the smaller are the patterns. Therefore, at least to a certain extent, the size of the patterns can be controlled by carefully choosing the reaction conditions. Also, electrochemical membrane systems exhibit a first-order phase transition (20). In many investigations, the degree of inhibition of an electron-transfer reaction serves as a measure of the intactness of the membrane. To be aware of the spatial instability discussed above is thus essential for understanding the dynamics of these lipid layers coupled to faradaic reactions. This, in turn, is the basis for using electrochemical membrane systems as models of biological membranes, e.g., in investigations of the role of the potential on the membrane-protein interactions (21, 22).

Turing's conditions are fulfilled in chemical reaction-diffusion systems only in exceptional cases, whereas the new class of Turing-type structures in electrochemical systems is predicted to arise quite generally. This finding opens prospects toward tailoring of patterned electrodes. It remains further to be examined whether the same mechanism is responsible for some structure formation phenomena in a biological environment where potential gradients exist.

References and Notes

1. A. M. Turing, *Philos. Trans. R. Soc. London* **237**, 37 (1952).
2. R. Kapral, K. Showalter, Eds., *Chemical Waves and Patterns* (Kluwer, Dordrecht, Netherlands, 1995).
3. J. D. Murray, *Mathematical Biology* (Springer, Berlin, 1990).
4. G. Nicolis, *Introduction to Nonlinear Science* (Cambridge Univ. Press, Cambridge, 1995).
5. J. Ross, A. P. Arkin, S. C. Müller, *J. Chem. Phys.* **99**, 10417 (1995).
6. V. Castets, E. Dulos, J. Boissonade, P. deKepper, *Phys. Rev. Lett.* **64**, 2953 (1990).
7. I. R. Epstein, I. Lengyel, S. Kádár, M. Kagan, M. Yokoyama, *Physics A* **188**, 26 (1992).
8. Q. Ouyang, H. L. Swinney, *Nature* **352**, 610 (1991).
9. I. Lengyel, I. R. Epstein, *Proc. Natl. Acad. Sci. U.S.A.* **89**, 3977 (1992).
10. N. Mazouz, K. Krischer, *J. Phys. Chem. B* **104**, 6081 (2000).
11. The term reflects the fact that when connecting the ends of the two stable states of the bistable region of the $I-\Phi_{DL}$ curve, the two stable branches together with the connecting line form an S shape. A second type of bistable $I-\Phi_{DL}$ curve gives rise to a Z shape (compare with Fig. 2C).
12. G. Flätgen et al., *Science* **269**, 668 (1995).
13. H. Striegler, thesis, Universität Ulm, Germany (1998).
14. N. Mazouz, G. Flätgen, K. Krischer, *Phys. Rev. E* **55**, 2260 (1997).
15. M. Hildebrand, A. Mikhailov, G. Ertl, *Phys. Rev. E* **68**, 5483 (1998).
16. B. A. Huberman, *J. Chem. Phys.* **65**, 2013 (1976).
17. A. Mikhailov, G. Ertl, *Chem. Phys. Lett.* **238**, 104 (1995).

18. J. Verdasca, P. Borckmans, G. Dewel, *Phys. Rev. E* **52**, R4616 (1995).
19. Reviewed in C. Buess-Herman, *Prog. Surf. Sci.* **46**, 335 (1994).
20. D. Bizzotto, A. Nelson, *Langmuir* **14**, 6269 (1998).
21. D. Bizzotto, E. Wang, Y. Yang, *J. Electroanal. Chem.* **480**, 233 (2000).
22. M. Rueda et al., *Langmuir* **15**, 3672 (1999).
23. We are grateful to D. M. Kolb and H. Striegler for

discussions on camphor adsorption on Au electrodes and to A. Martin (Fritz-Haber-Institut) for preparing the Au films. Supported by the Deutsche Forschungsgemeinschaft, in the framework of the Sfb 555/B4.

28 November 2000; accepted 13 February 2001
 Published online 22 February 2001;
 10.1126/science.1057830
 Include this information when citing this paper.

Biogenic Carbon Cycling in the Upper Ocean: Effects of Microbial Respiration

Richard B. Rivkin^{1*} and Louis Legendre²

Food-web processes are important controls of oceanic biogenic carbon flux and ocean-atmosphere carbon dioxide exchange. Two key controlling parameters are the growth efficiencies of the principal trophic components and the rate of carbon remineralization. We report that bacterial growth efficiency is an inverse function of temperature. This relationship permits bacterial respiration in the euphotic zone to be computed from temperature and bacterial production. Using the temperature-growth efficiency relationship, we show that bacterial respiration generally accounts for most community respiration. This implies that a larger fraction of assimilated carbon is respired at low than at high latitudes, so a greater proportion of production can be exported in polar than in tropical regions. Because bacterial production is also a function of temperature, it should be possible to compute euphotic zone heterotrophic respiration at large scales using remotely sensed information.

The net flux of CO₂ between the atmosphere and ocean is controlled, in large part, by the balance among three key food-web processes: carbon uptake by phytoplankton photosynthesis (PP, net primary production), its remineralization back to CO₂ (CR, community heterotrophic respiration in the euphotic zone), and the export (E) of dissolved and particulate biogenic carbon (BC) toward the ocean depths. Although phytoplankton production and, to a lesser extent, export are reasonably well defined for large ocean areas (1), the regional estimates of respiration that are necessary to constrain both export (E = PP - CR) and the net ocean-atmosphere exchange of CO₂ are often lacking (2). Community respiration, of which bacterial respiration (BR) can represent a large proportion [~50 to >90% (3-5)], can exceed primary production in some ocean regions (6-9). Hence, bacterial respiration may constrain the estimates of both carbon remineralization and biogenic carbon export in the upper ocean (7). Because of methodological difficulties, bacterial respiration is usually not measured directly and is instead computed from bacterial produc-

tion (BP) and an assumed value of bacterial growth efficiency (BGE)

$$BGE = BP/B_{DOC} \quad (1)$$

Bacterial growth efficiency is the ratio of bacterial production to substrate assimilated (B_{DOC}), and since the assimilated dissolved organic carbon (DOC) is used for both the synthesis of bacterial biomass and is respired (i.e., B_{DOC} = BP + BR), bacterial growth efficiency can also be computed as

$$BGE = BP/(BP + BR) \quad (2)$$

Hence

$$BR = (BP/BGE) - BP \quad (3)$$

The estimation of bacterial respiration from Eq. 3 has been limited until now because of large variations reported for bacterial growth efficiencies [0.01 to ~0.7 (5, 9, 10)]. These variations introduce large uncertainties into the computation of bacterial respiration. For example, for the twofold range of growth efficiencies (e.g., 0.25 to 0.5) assumed in many studies (6, 9, 11), respiration would change by threefold. It follows that the use of a realistic bacterial growth efficiency is crucial to constraining rates and patterns of carbon remineralization, food-web fluxes of biogenic carbon, and ocean-atmosphere flux of CO₂ (2, 6, 8).

We carried out a comprehensive review of the literature on bacterial growth efficiency (12, 13) and found a significant ($P < 0.001$) inverse

¹Ocean Sciences Centre, Memorial University of Newfoundland, St. John's, Newfoundland A1C 5S7, Canada. ²Laboratoire d'Océanographie de Villefranche, Boîte Postale 28, 06234 Villefranche-sur-Mer Cedex, France.

*To whom correspondence should be addressed. E-mail: rivkin@mun.ca